

Comparisons of MHD Propeller Model with Observations of Cataclysmic Variable AE Aqr

A. A. Blinova^{1,2}, M. M. Romanova^{1,2*}, G. V. Ustyugova³, A. V. Koldoba⁴, R. V. E. Lovelace^{1,2,5}

¹Department of Astronomy, Cornell University, Ithaca, NY 14853-6801

²Carl Sagan Institute, Cornell University, Ithaca, NY 14853-6801

³Keldysh Institute for Applied Mathematics, Moscow, 125047, Russia

⁴Moscow Institute of Physics and Technology, Dolgoprudny, Moscow Region, 141700, Russia

⁵Department of Applied and Engineering Physics, Cornell University, Ithaca, NY 14853-6801

February 11, 2022

ABSTRACT

We have developed a numerical MHD model of the propeller candidate star AE Aqr using axisymmetric magneto-hydrodynamic (MHD) simulations. We suggest that AE Aqr is an intermediate polar-type star, where the magnetic field is relatively weak and an accretion disc may form around the white dwarf. The star is in the propeller regime, and many of its observational properties are determined by the disc-magnetosphere interaction. Comparisons of the characteristics of the observed versus modelled AE Aqr star show that the model can explain many observational properties of AE Aqr. In a representative model, the magnetic field of the star is $B \approx 3.3 \times 10^5$ G and the time-averaged accretion rate in the disc is 5.5×10^{16} g/s. Most of this matter is ejected into conically-shaped winds. The numerical model explains the rapid spin-down of AE Aqr through the outflow of angular momentum from the surface of the star to the wind, corona and disc. The energy budget in the outflows, 9×10^{33} erg/s, is sufficient for explaining the observed flaring radiation in different wavebands. The time scale of ejections into the wind matches the short time scale variability in the light curves of AE Aqr.

1 INTRODUCTION

AE Aqr is a nova-like cataclysmic variable (CV). It consists of a magnetic white dwarf and a late-type companion star with a spectral type of K3-K5. The binary has a relatively long period of 9.88 hours. It is widely believed that the companion star's atmosphere fills its Roche lobe and matter flows out of the companion's Roche lobe to the white dwarf (Casares et al. 1996). Pulsations with a period of 33.08 s were detected in optical (Patterson 1979), UV (e.g., Eracleous et al. 1994), soft X-ray (Patterson et al. 1980), and hard X-ray (Kitaguchi et al. 2014) wavebands.

AE Aqr could be classified as a typical intermediate polar (DQ Her) type CV, except that it has a number of unusual properties: (1) It shows flaring radiation in optical, ultraviolet and X-ray bands, which are all correlated with each other (e.g., Patterson 1979; Mauche et al. 2012); (2) Flaring radiation in the radio band shows a non-thermal spectrum typical for electrons radiating in a magnetized plasma (Bastian et al. 1988). Authors compared the radio flares in AE Aqr with those of the micro-quasar Cyg X-3; (3) The star is spinning down rapidly, at a rate of $\dot{P} = 5.64 \times 10^{-14}$ s s⁻¹, which corresponds to a high spin-down power of $\dot{E}_{\text{sd}} \approx 6 \times 10^{33} I_{50}$ erg/s (where $I_{50} = I/10^{50}$ gcm²) (De Jager et al. 1994); (4) The estimated accretion luminosity, $\dot{E}_{\text{acc}} \lesssim 10^{32}$ erg/s (e.g.,

Mauche 2006), is much lower than the spin-down power; (5) The H_{α} spectral lines are strongly variable and indicate the presence of outflows. The Doppler tomograms based on the analysis of these lines¹ are different from the tomograms of other intermediate polars, which typically indicate the presence of an accretion disc (e.g., Marsh et al. 1990). No signatures of a disc were observed in the AE Aqr tomograms (see Fig. 10 from Welsh et al. 1998).

Different models were proposed to explain the observational properties of AE Aqr. In one type of models, it is suggested that the magnetic field of AE Aqr is very large, $B_s \approx 5 \times 10^7$ G, and the white dwarf spins down due to the magneto-dipole radiation, as in the case of pulsars (e.g., Ikhsanov 1998, 2006). In the second type of models, it is suggested that the magnetic field of the star is typical for that of intermediate polars, $B \lesssim 2 \times 10^6$ G (Warner 1995), and the star spins down due to the interaction of the rapidly-rotating magnetosphere with the surrounding matter in the propeller regime (e.g., Eracleous & Horne 1996).

¹ Note that Doppler tomography implicitly assumes that emission is optically thin and bound to the orbital plane of the binary (e.g., Schwobe et al. 1999). Therefore, Doppler tomography is not the optimal tool for investigating the presence of winds.

The apparent lack of an accretion disc in the Doppler tomograms led to the suggestion that an accretion disc does not form; instead, matter flows from the secondary star in a stream of blobs, which interact with the magnetosphere of the WD directly without forming a disc (e.g., King 1993; Wynn & King 1995; Wynn et al. 1997). In their model, blobs of matter interact with the WD ballistically, and a diffusive term has been added to the equations to describe the interaction of the blobs with the magnetosphere of the star. The flaring radiation in different wavebands is explained by the collisions of blobs during their exit path from the white dwarf (Welsh et al. 1998).

Meintjes & de Jager (2000) suggested that a stream of matter flowing from the secondary star interacts with the external layers of the magnetosphere, loses its angular momentum and forms a ring or a small disc around the white dwarf. The matter distribution in this ring is strongly inhomogeneous. Recent 3D MHD simulations of matter flow in AE Aqr have shown that a stream of matter flowing from the secondary star collides with itself after the 1st turn around the white dwarf, forming a ring around it that subsequently forms a turbulent disc (Isakova et al. 2016). Next, the matter of the disc is ejected by the magnetosphere of the WD due to the propeller mechanism. In their model, the magnetic field of the WD is large, 50MG, which leads to a rapid ejection of the inner disc matter by the large, rapidly-rotating magnetosphere.

Overall, it is reasonable to suggest that, in the cases of IP-scale magnetic fields, some kind of disc may form around the white dwarf in AE Aqr. The disc may have unusual properties compared with the discs around non-propelling stars: it may be much smaller than standard discs in IPs, which are thought to have sizes of Roche lobes. It may also be temporary due to the propeller action.

The propeller regime is expected in AE Aqr, and various observational properties may be connected with this regime. However, the disc-magnetosphere interaction in the propeller regime is a complex phenomenon, and has not been sufficiently studied. It has been investigated in a few theoretical works on spherical accretion (e.g., Illarionov & Sunyaev 1975) and disc accretion (Lovelace et al. 1999). However, only restricted numerical models of the propeller regime have been developed so far. Wang & Robertson (1985) studied the propeller regime in two-dimensional numerical simulations using polar coordinates, and thus studied the processes in the equatorial plane. They observed that the matter of the inner disc interacts with the magnetosphere of the star due to the magnetic interchange instability (see also Arons & Lea 1976). No outflows were observed due to the two-dimensional polar geometry of their coordinate system.

The propeller regime has also been studied in axisymmetric simulations (Ustyugova et al. 2006; Romanova et al. 2005, 2009, 2018; Lii et al. 2014). These simulations have shown that the disc-magnetosphere interaction is a strongly non-stationary process, where the inner disc oscillates and most of the matter is ejected into the outflows from the disc-magnetosphere boundary, while a smaller amount of matter accretes onto the star. The WD spins down due to the outflow of angular momentum into the matter- and magnetically-dominated winds. This model can potentially explain the different observational properties of CV AE Aqr. In this paper, we have developed a propeller model of a star with parameters

corresponding to those of AE Aqr, calculated the properties of the modelled star and compared them with the observed properties of AE Aqr.

In Sec. 2, we describe our model of AE Aqr. In Sec. 3, we compare our model with the observations. In Sec. 4, we summarize our results. In Appendix A, we provide the details of our numerical model.

2 PROPELLER MODEL OF AE AQR

2.1 Preliminary estimates

To model the propeller regime in AE Aqr, we take the mass and radius of the white dwarf to be $M_s = 0.8M_\odot$ and $R_s = 7 \times 10^3$ km, respectively (e.g., Mauche et al. 2012). The period of stellar rotation, $P_s = 33.08$ s, corresponds to a corotation radius of

$$r_{\text{cor}} = \left(\frac{GM_s P_s^2}{4\pi^2} \right)^{1/3} \approx 1.44 \times 10^4 \text{ km} \approx 2.05 R_s. \quad (1)$$

We suggest that a disc forms around the WD. The luminosity associated with accretion onto the stellar surface is low, and is estimated to be $\dot{E}_s \lesssim 10^{32}$ erg/s (e.g., Mauche 2006). It is connected with the matter flux onto the star as

$$\dot{E}_s = \eta \frac{\dot{M}_s G M_s}{R_s} \approx 1.53 \times 10^{31} \eta \dot{M}_{s15} \frac{\text{erg}}{\text{s}}, \quad (2)$$

where $\dot{M}_{s15} = \dot{M}_s / 10^{15}$ g/s and the coefficient η takes into account the fact that matter may fall from the finite distance r . For example, if matter falls from the distance of the corotation radius, $r_{\text{cor}} \approx 2R_s$, then $\eta = 0.5$. The corresponding accretion rate onto the star is:

$$\dot{M}_s = \eta \frac{\dot{E}_s R_s}{G M_s} \approx 1.31 \times 10^{15} \frac{\dot{E}_{s32}}{\eta_{0.5}} \frac{\text{g}}{\text{s}}, \quad (3)$$

where $\dot{E}_{s32} = \dot{E}_s / 10^{32}$ erg/s and $\eta_{0.5} = \eta / 0.5$.

The accretion disc is stopped by the magnetosphere of the star at the radius of r_m , where the matter stress in the disc is equal to the magnetic stress in the magnetosphere. This condition can be approximately described by the formula for the Alfvén radius, obtained for non-rotating stars (e.g., Pringle & Rees 1972; Ghosh & Lamb 1978):

$$r_m = k_m \frac{\mu_s^{4/7}}{(2G M_s \dot{M}_d^2)^{1/7}} \approx 2.52 \times 10^4 k_m B_5^{4/7} \dot{M}_{d17}^{-2/7} \text{ km}, \quad (4)$$

where μ_s is the magnetic moment of the WD and \dot{M}_d is the accretion rate in the disc (which, in the propeller regime, is larger than the accretion rate onto the star, \dot{M}_s); $k_m \sim 1$ is a dimensionless coefficient. $B_5 = B_s / 10^5$ G is the normalized magnetic field of the WD, and $\dot{M}_{d17} = \dot{M}_d / 10^{17}$ g/s is the normalized accretion rate in the disc.

To estimate the magnetospheric radius in AE Aqr, one needs to know the accretion rate \dot{M}_d , which is not well known². We suggest that $k_m = 1$ and the accretion rate in the disc is $\dot{M}_d = 10^{17}$ g/s to obtain the magnetospheric radius,

² For example, Pearson et al. (2003) estimated the mass transfer rate from the donor star as $\dot{M} = 3 \times 10^{17}$ g/s.

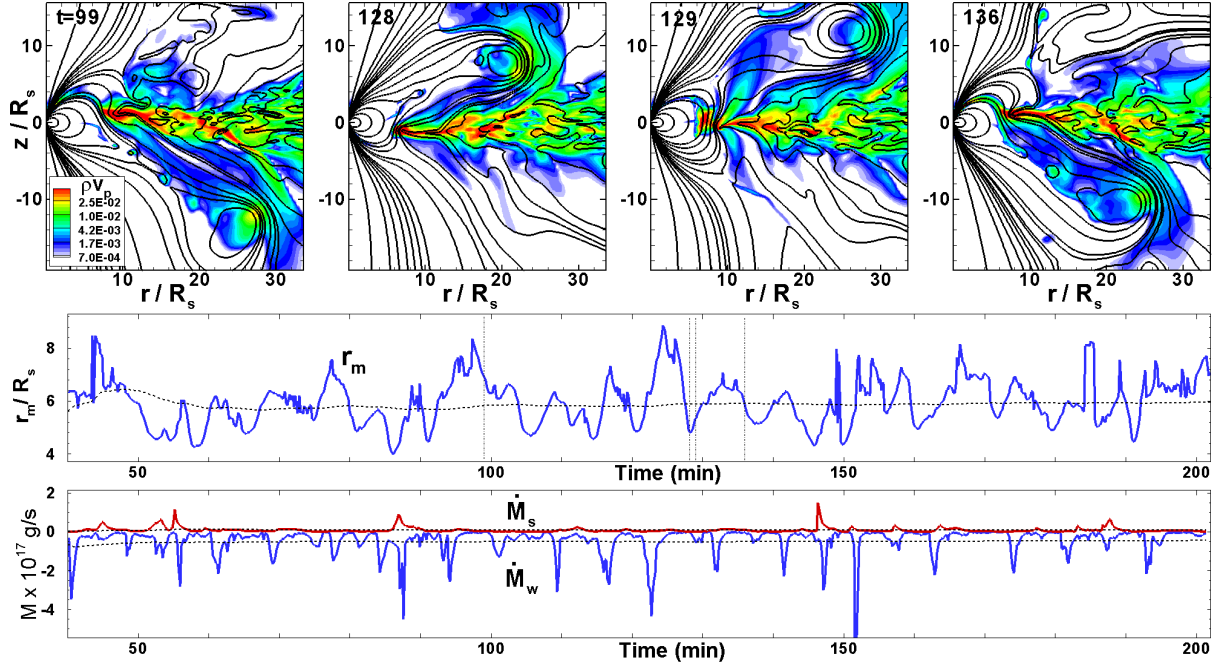


Figure 1. *Top row:* A two-dimensional picture of matter flow in the model $\mu 60$, shown at several moments in time. The colour background shows the matter flux density and the lines are sample field lines. *Middle row:* Variation of the inner disc radius, r_m , scaled to the radius of the star, R_s . *Bottom row:* Variation of matter fluxes at the stellar surface, \dot{M}_s , and into the wind, \dot{M}_w . Dashed lines show the time-averaged values. Vertical lines show the moments in time corresponding to the top panels.

$r_m \approx 3.60 B_5^{4/7} R_s$. Taking two reference values for the magnetic field of IPs, $B_s = 10^5$ G and $B_s = 10^6$ G, we obtain $r_m \approx 3.60 R_s$ and $r_m \approx 13.43 R_s$, respectively. In both cases, the magnetospheric radius is larger than the corotation radius, $r_{\text{cor}} = 2R_s$, and the star is in the propeller regime. However, the strengths of the propellers are different.

The strength of a propeller is often measured by the fastness parameter, ω_s (e.g. Ghosh 2007), which is the ratio of the angular velocity of the star, Ω_s , to the angular velocity at the inner disc, Ω_d : $\omega_s = \Omega_s / \Omega_d$. In the case of a Keplerian disc, $\Omega_d = \sqrt{GM_s / r_m^3}$, and the fastness parameter can be re-written in the following form:

$$\omega_s = \left(\frac{r_m}{r_{\text{cor}}} \right)^{3/2} \approx 2.32 B_5^{6/7} \dot{M}_{d17}^{-3/7}. \quad (5)$$

Using the reference values for the accretion rate, $\dot{M}_{d17} = \dot{M}_d / 10^{17} \text{ g/s}$, and for the magnetic field, $B_s = 10^5$ G and $B_s = 10^6$ G, we obtain the values of the fastness parameter, $\omega_s \approx 2.3$ and $\omega_s \approx 16.6$, respectively. These estimates are helpful in restricting the values of the fastness parameter in the modelling of AE Aqr.

2.2 Axisymmetric MHD Simulations of AE Aqr

As a base, we use the axisymmetric model of the propeller regime developed in our group (e.g., Lii et al. 2014; Romanova et al. 2018). We start with the initial conditions that are expected in disc-accreting propelling stars: the simulation region consists of (a) a star with mass M_s , radius R_s and magnetic field B_s ; (b) an accretion disc that is cold and dense, and has an aspect ratio of $H/r \approx 0.15$ (H is the initial half-thickness of the disc); (c) a low-density and high-temperature corona, which occupies the rest of the simulation region (i.e.,

the space above and below the disk and the star; see left panel of Fig. 1 from Romanova et al. 2018). Initially, the matter in the disc and in the corona are in rotational equilibrium, in which the density and pressure distributions are derived from the balance of the gravitational, pressure gradient and centrifugal forces (Romanova et al. 2002).

The disc is turbulent. The turbulence is driven by the magneto-rotational instability (MRI, e.g., Balbus & Hawley 1991; Stone et al. 1996; Armitage 1998; Hawley 2000), which is initiated by a weak poloidal magnetic field placed inside the disc. In our model, the accretion rate corresponds to an effective α -parameter of $\alpha_{\text{mag}} \approx 0.02 - 0.04$. A diffusivity term has been added to the code, with the coefficient of diffusivity constructed in analogy with α -viscosity (Shakura & Sunyaev 1973): $\eta_d = \alpha_d c_s H$, where c_s is the sound speed and α_d is a dimensionless parameter.

In our models, we suggest that the 3D instabilities should provide high diffusivity, and we use $\alpha_d = 1$ at radii $r < 7R_s$, where the disc typically interacts with the magnetosphere, and $\alpha_d = 0$ in the rest of the disc (to avoid suppressing the MRI-driven turbulence). The star rotates with an angular velocity of Ω_s such that the magnetosphere rotates more rapidly than the inner disc, and the star is in the propeller regime.

The models are calculated in dimensionless variables. The conversion procedure for dimensionalization and other details of the model are provided in Appendix A3.

To model AE Aqr, we take the corotation radius $r_{\text{cor}} = 2R_s$ (see Eq. 1), or $\tilde{r}_{\text{cor}} = 2$ in dimensionless units (see Appendix A3), and calculate all models for this corotation radius. Since the magnetic field of AE Aqr is not known, we model propellers of different magnetospheric radii r_m . To do so, we vary the parameter μ , which we call the dimensionless

Model	$\tilde{\mu}$	$\langle \tilde{r}_m \rangle$	$\langle \tilde{r}_m \rangle / \tilde{r}_{\text{cor}}$	$\langle \omega_s \rangle$	$\langle \tilde{M}_s \rangle$	$\langle \tilde{M}_w \rangle$	f_{eff}
$\tilde{\mu}30$	30	5.0	2.5	3.9	0.17	0.76	0.82
$\tilde{\mu}60$	60	5.9	3.0	5.1	0.22	1.24	0.85

Table 1. Dimensionless values obtained in two models of the strong propeller regime, where the corotation radius $r_{\text{cor}} = 2R_s$. Parameter $\tilde{\mu}$ determines the final values of the time-averaged magnetospheric radii, $\langle \tilde{r}_m \rangle$, and the fastness parameter, ω_s . Here, $\langle \tilde{M}_s \rangle$ is the time-averaged matter flux onto the star; $\langle \tilde{M}_w \rangle$ is the matter flux into the wind, calculated through the surface $S(r = 10, z = \pm 10)$ at condition $v_{\text{min}} > 0.1v_{\text{esc}}$; f_{eff} is the propeller efficiency.

magnetic moment of the star³. We have developed numerical models for $\tilde{\mu} = 30$ and 60 and obtained different magnetospheric radii (and therefore different fastness values ω_s).

We observed that, in both models, the inner disc strongly oscillates and most of the inner disc matter is redirected into the outflows. The top panels of Fig. 1 show the matter flux density and sample field lines in the model $\tilde{\mu}60$. One can see that the magnetic field lines inflate and open, and some of the matter is ejected into conically-shaped outflows. Matter is ejected at approximately 45 – 50 degrees relative to the rotational axis. Ejections above and below the equatorial plane alternate.⁴

The disc-magnetosphere interaction occurs in a cyclic manner, where episodes of matter accumulation in the inner disc are followed by events of matter ejection into the winds and simultaneous accretion of matter onto the star (see, e.g., Lii et al. 2014, see also Goodson et al. 1997).

We find the dimensionless magnetospheric radius \tilde{r}_m from the simulations using the balance of magnetic and matter stresses, $\tilde{B}^2/8\pi = \tilde{P} + \rho\tilde{v}^2$, where \tilde{B} , \tilde{P} and $\tilde{\rho}$ are the magnetic field, pressure and density of matter in the equatorial plane, respectively (Romanova et al. 2018). This formula provides the instantaneous value of \tilde{r}_m . The middle row of Fig. 1 shows that the inner disc strongly oscillates and the magnetospheric radius \tilde{r}_m varies with time, which is why we calculate the time-averaged magnetospheric radius,

$$\langle \tilde{r}_m(t) \rangle = \frac{\int_{t_i}^t dt' \tilde{r}_m(t')}{\int_{t_i}^t dt'}. \quad (6)$$

The dashed line in the middle row of Fig. 1 shows the time-averaged value $\langle \tilde{r}_m \rangle$. We also calculated the time-averaged fastness parameter,

$$\langle \omega_s \rangle = \left(\frac{\langle \tilde{r}_m \rangle}{\tilde{r}_{\text{cor}}} \right)^{\frac{3}{2}}. \quad (7)$$

Tab. 1 shows the time-averaged magnetospheric radius, $\langle \tilde{r}_m \rangle$, the ratio $\langle \tilde{r}_m \rangle / \tilde{r}_{\text{cor}}$ and the fastness parameter $\langle \omega_s \rangle$ for both models. We obtained that the time-averaged size of the magnetosphere increases with $\tilde{\mu}$, and is $\langle r_m \rangle \approx 5, 5.9$ for models $\tilde{\mu}30$, and $\tilde{\mu}60$, respectively. The fastness parameter also increases systematically: $\omega_s = 3.9, 5.1$ for the same models, respectively. Both values of $\langle \omega_s \rangle$ are within the interval of

fastnesses, $2.3 \lesssim \omega_s \lesssim 16.6$, expected in IPs with magnetic fields in the range of $B = 10^5 - 10^6$ G (see Eq. 7)⁵.

Simulations performed in dimensionless form provide different values that can be used for the subsequent development of a dimensional model of AE Aqr, and for comparisons with observations. The bottom row of Fig. 1 shows the matter fluxes onto the star, \tilde{M}_s , and into the wind, \tilde{M}_w . One can see that the fluxes strongly oscillate. Matter accretes onto the star in rare bursts, because most of time accretion is blocked by the centrifugal barrier of the rapidly-rotating magnetosphere. Ejections into the wind (blue line) are more frequent than accretion events (red line). To characterize each model, we introduce the time-averaged matter fluxes, which are calculated using a formula similar to Eq. 6. The dashed lines show the time-averaged values of the matter fluxes to the star, $\langle \tilde{M}_s \rangle$, and to the wind, $\langle \tilde{M}_w \rangle$. Simulations show that most of the inner disc matter is ejected into the winds.

Tab. 3 also shows the efficiency of the propeller:

$$f_{\text{eff}} = \frac{\langle \tilde{M}_w \rangle}{\langle \tilde{M}_s \rangle + \langle \tilde{M}_w \rangle}. \quad (8)$$

One can see that propeller efficiency is $f_{\text{eff}} = 0.82, 0.85$ for $\tilde{\mu} = 30, 60$, respectively. That is, 82 – 85 per cent of the disc matter is ejected into the wind, while 18% – 15% accretes onto the star⁶.

Next, we use the data obtained in our dimensionless models to develop the dimensional models of AE Aqr. To obtain a dimensional value A , we take the dimensionless value \tilde{A} from the simulations, and multiply it by the reference value A_0 : $A = \tilde{A}A_0$. We derive the reference values A_0 using our standard procedure described in Appendix A3.

3 COMPARISONS OF MODEL WITH OBSERVATIONS OF AE AQR

Below, we compare the different values calculated in our model with the values observed in AE Aqr.

³ In our dimensionless model, the variation of parameter $\tilde{\mu}$ can be interpreted as either the variation of the stellar magnetic moment, μ_s , or the variation of the accretion rate in the disc, \dot{M}_d . A variation of both values leads to the variation in r_m as $\sim (\mu_s^2/\dot{M}_d)^{1/7}$.

⁴ In our axisymmetric simulations, matter is ejected into an azimuthally-symmetric cone. In a more realistic, three-dimensional world, we would expect non-axisymmetric ejections of blobs of matter, which would shoot out in different azimuthal directions.

⁵ Note that we currently cannot model propellers with magnetospheric radii $\langle r_m \rangle \gtrsim 7R_s$, because in the cases of large magnetospheres, the density of the plasma inside the magnetosphere becomes very low, and the time-step in the simulations becomes too small. As a result, in the models with a corotation radius of $r_{\text{cor}} \approx 2R_s$, we can only model propellers with values of $\omega_s \lesssim 6 - 7$.

⁶ We should note that our *axisymmetric* model may provide too high accretion rate onto a star, because we model the (unknown) rate of penetration of the disc matter through the magnetosphere by high diffusivity values in the region $r < 7R_s$.

3.1 Magnetic field of AE Aqr derived from comparisons of modelled and observed spin-down rates

In this section, we compare the spin-down rates obtained in our numerical model with the observed spin-down rate of $P_{\text{sd}} = 5.64 \times 10^{-14}$ s/s, and derive the possible values of the magnetic field.

The angular momentum of the star is $L_s = I_s \Omega_s$, where the value of the moment of inertia of the white dwarf is $I_s = k M_s R_s^2 = 1.57 \times 10^{50} k_{0.2} \text{gcm}^2$. The time-averaged spin-down rate can be estimated from the relation $\langle \dot{L}_{\text{sd}} \rangle = I_s \langle \dot{\Omega}_{\text{sd}} \rangle$, and can be re-written in the following form:

$$\begin{aligned} \langle \dot{P}_{\text{sd}} \rangle &= \frac{P_s \langle \dot{L}_{\text{sd}} \rangle}{I_s \Omega_s} = \frac{P_s^2 \langle \dot{L}_{\text{sd}} \rangle}{2\pi I_s} \approx \\ &\approx 1.05 \times 10^{-15} k_{0.2}^{-1} B_s^{-2} \tilde{\mu}_{60}^{-2} \langle \dot{L}_{\text{sd}} \rangle \frac{\text{s}}{\text{s}}. \end{aligned} \quad (9)$$

Table 2 shows the spin-down rates obtained in our models.

To derive the magnetic field of AE Aqr, we equate the spin-down rates $\langle \dot{P}_{\text{sd}} \rangle$ obtained in the simulations (see Eq. 9) with the observed spin-down rate. We obtain the magnetic field in the following form:

$$B_{\text{Psd}} \approx 7.33 \times 10^5 \tilde{\mu}_{60} k_{0.2}^{1/2} \langle \dot{L}_{\text{sd}} \rangle^{-1/2} \text{G}. \quad (10)$$

Tab. 2 shows the values of the magnetic field, B_{Psd} , which are $B_s \approx 2.8 \times 10^5$ and $B_s \approx 3.3 \times 10^5$ G, for models $\tilde{\mu}_{30}$, and $\tilde{\mu}_{60}$, respectively. One can see that the strength of the magnetic field increases slightly with $\tilde{\mu}$. It does depend on the moment of inertia coefficient, $k_{0.2}$, which can vary by a factor of ~ 2 (depending on the model of the white dwarf). Overall, these values are in the range of the magnetic field values estimated for IPs. Note that (Choi & Yi 2000) estimated a magnetic field of the white dwarf of 3×10^5 G on basis of the quiescent X-ray and UV emission. This value is very close to values obtained in our models. Note that this field is much lower than the field 5×10^7 G used in other type of models (e.g., Ikhsanov et al. 2004, and references therein).

The time-averaged spin-down power of the star:

$$\begin{aligned} \langle \dot{E}_{\text{sd}} \rangle &= \langle \dot{L}_{\text{sd}} \rangle \Omega_s = \dot{L}_0 \langle \dot{L}_{\text{sd}} \rangle 2\pi / P_s \approx \\ &\approx 1.80 \times 10^{32} \tilde{\mu}_{60}^{-2} B_s^{-2} \langle \dot{L}_{\text{sd}} \rangle \text{erg/s}. \end{aligned} \quad (11)$$

corresponds to the spin-down rate $\dot{E}_{\text{sd}} \approx 6 \times 10^{33} I_{50} \text{erg/s}$ $\approx 9.4 \times 10^{33} \text{erg/s}$, derived from observations (see Tab. 2).

These comparisons show that the propeller model offers a good explanation for the observed spin-down properties of the star. However, we cannot yet select one specific model over another, because both models can explain the observations, although at slightly different values of the stellar magnetic field.

3.2 Matter fluxes to the star and to the wind

We can now calculate the dimensional values of the matter fluxes onto the star and into the wind. We take the reference value, \dot{M}_0 , from Eq. A1 and take the dimensionless values from Tab. 1 to obtain the time-averaged matter fluxes to the star (subscript 's') and to the wind (subscript 'w'):

$$\langle \dot{M}_{s,w} \rangle = \dot{M}_0 \langle \tilde{M}_{s,w} \rangle \approx 3.47 \times 10^{15} \tilde{\mu}_{60}^{-2} B_s^{-2} \langle \tilde{M}_{s,w} \rangle \text{g/s}. \quad (12)$$

Substituting in the values of the magnetic field from Tab. 2, we obtain the values of the matter fluxes (see Tab. 3). The table also shows the time-averaged total matter flux through the disc: $\langle \dot{M}_d \rangle = \langle \dot{M}_s \rangle + \langle \dot{M}_w \rangle$. One can see that the matter flux in the disc decreases when parameter $\tilde{\mu}$ increases.

The matter flux in the disc obtained in our models, $4.45 \times 10^{16} \text{g/s} \lesssim \langle \dot{M}_d \rangle \lesssim 1.0 \times 10^{17} \text{g/s}$, is comparable to the mass transfer rates expected in nova-like CVs with orbital periods of ~ 10 hours: $\sim 1.0 \times 10^{17} \text{g/s}$ (e.g., Dhillion 1996).

We use Eq. 2 and our values of $\langle \dot{M}_s \rangle$ to estimate the luminosity associated with accretion onto the star, $\langle \dot{E}_s \rangle$. Tab. 3 shows the values of luminosity. The luminosity $\langle \dot{E}_s \rangle$ is more than 10 times larger than the accretion luminosity deduced from the observations: $\dot{E}_{\text{acc}} \lesssim 10^{32} \text{erg/s}$. The last column of Tab. 3 shows the ratio between the accretion luminosity obtained in our models and the observed luminosity of $\dot{E}_s \approx 10^{32} \text{erg/s}$. One can see that the accretion luminosity obtained in our models is 6 – 14 times higher than the observed one.

The relatively high accretion rate onto the star may be connected with the axisymmetry of our model and our high diffusivity value ($\alpha_d = 1$) taken at the disc-magnetosphere boundary. At lower values of α_d , the accretion rate is expected to be lower. We also should note that to support MHD simulations, a small amount of matter (floor density matter) is added to the parts of the magnetosphere with the largest values of the magnetic-to-matter pressure density. This matter may also contribute to the accretion rate onto a star.

3.3 Velocities of matter in the wind

Welsh et al. (1998) performed high-speed spectrophotometric observations of AE Aqr in the H_α spectral line and found that the spectral line varies rapidly in both red and blue wings. Doppler signatures from variable lines show that the red and blue wings span from 250 km/s to 1,600 km/s, with a significant amount of radiation which comes from the matter that flows at radial velocities of $\lesssim 500$ km/s, and a smaller amount of matter flowing at higher velocities (see Figures 8-10 from Welsh et al. 1998). Below, we analyze the distribution of velocities in our model, and discuss the possible locations where this flaring radiation may originate.

First, we calculate the total velocity of matter flow in different parts of our simulation region, $v_{\text{tot}} = \sqrt{v_r^2 + v_z^2 + v_\phi^2}$, where v_r , v_z and v_ϕ are the components of velocity in r , z and ϕ directions, respectively. Fig. 2 (top right panel) shows the distribution of total velocity during a typical propeller ejection. One can see that the total velocity is high in the area of propeller ejecta, $v_{\text{tot}} \sim 1,000 - 1,200 \text{km/s}$ (see region A in the plot), and is lower in region B, between the disc and the ejecta. Velocity is lowest in the disc, with a minimum value of $v_{\text{tot}} \approx (650 - 700) \text{km/s}$. These velocities are too high to explain the low-velocity component observed in the Doppler shifts of the H_α spectral line. The lowest velocity is associated with Keplerian velocity of the disc matter. This velocity decreases with distance from the star as $v_K = \sqrt{GM_s/R_s} \approx 872(r/20)^{-0.5}$ (see also left panel of Fig. 3), and reaches the value of $v_\phi \sim 500 \text{km/s}$ at the distance of $r \approx 61 R_s$, which is approximately twice as large as our simulation region in the radial direction.

Next, we investigate the poloidal velocities, $v_p =$

Model	$\langle \dot{P}_{\text{sd}} \rangle$ (s/s)	B_{Psd} (G)	$\langle \tilde{L}_{\text{sd}} \rangle$	$\langle \dot{E}_{\text{sd}} \rangle$ (erg/s)
$\tilde{\mu}30$	$7.06\text{E-}15 B_5^2 / k_{0.2}$	$2.83\text{E}5 \sqrt{k_{0.2}}$	1.68	$9.69\text{E}33 k_{0.2}$
$\tilde{\mu}60$	$5.20\text{E-}15 B_5^2 / k_{0.2}$	$3.29\text{E}5 \sqrt{k_{0.2}}$	4.95	$9.64\text{E}33 k_{0.2}$

Table 2. Values of the magnetic field, B_{Psd} , derived from the comparisons of the spin-down rates, \dot{P}_{sd} . $\langle \dot{E}_{\text{sd}} \rangle$ is the calculated value of spin-down power.

Model	$\langle \dot{M}_s \rangle$ (g/s)	$\langle \dot{M}_w \rangle$ (g/s)	$\langle \dot{M}_d \rangle$ (g/s)	f_{eff}	$\langle \dot{E}_s \rangle$ (erg/s)	$\langle \dot{M}_s \rangle / \dot{M}_{\text{obs}}$
$\tilde{\mu}30$	$1.89\text{E}16 k_{0.2}$	$8.41\text{E}16 k_{0.2}$	$1.03\text{E}17 k_{0.2}$	0.82	$2.88\text{E}33 k_{0.2} \eta$	$14.4 k_{0.2} \eta_{0.5}$
$\tilde{\mu}60$	$8.24\text{E}15 k_{0.2}$	$4.65\text{E}16 k_{0.2}$	$5.47\text{E}16 k_{0.2}$	0.85	$1.25\text{E}33 k_{0.2} \eta$	$6.24 k_{0.2} \eta_{0.5}$

Table 3. The time-averaged matter fluxes onto the star, $\langle \dot{M}_s \rangle$, into the wind, $\langle \dot{M}_w \rangle$, and in the disc, $\langle \dot{M}_d \rangle$. f_{eff} is the efficiency of the propeller. $\langle \dot{E}_s \rangle$ is the energy flux associated with accretion onto the star and calculated using Eq. 2; \dot{M}_{obs} is calculated using the observed luminosity: $\dot{E}_{\text{obs}} \approx 10^{32}$ erg/s.

$\sqrt{v_r^2 + v_z^2}$. Fig. 2 shows that the poloidal velocities (vectors in the plot) are largest in the area of the propeller ejecta (region A in the plot). They are smaller in the disc wind (region B). There is also region C (closer to the axis), where velocities may be very high. However, the density in this region is very low (see distribution of densities in the top left panel of the same figure), and this region does not contribute much to the matter flux. Analysis of the poloidal matter fluxes, ρv_p , shows that most of the matter flows in the regions A (higher velocities) and B (lower velocities).

The question arises whether the ejected matter moves with super-escape velocities. For this analysis, we study the distribution of poloidal velocities with distance from the star. We surround a star with cylindrical boxes of radii r and heights $z = \pm r$, and search for the maximum poloidal velocity, v_{max} , at the cylindrical boxes $(r, z = \pm r)$ ⁷. The bottom panel of Fig. 2 shows variation of the maximum poloidal velocity with time at the cylindrical boxes with radii $(r, z) = (20R_s, \pm 20R_s)$ (solid blue line) and $(r, z) = (30R_s, \pm 30R_s)$ (long-dashed line). One can see that the maximum velocity varies between small values, much smaller than the escape velocity, and large values, which are 2-3 times larger than the escape velocity. This analysis shows that the ejected matter is not gravitationally bound, and will continue to move further away to larger distances from the star.

Another question is whether matter moves from the star with acceleration or deceleration. To analyze the variation of poloidal velocity with distance from the star, we calculate the time-averaged maximum poloidal velocity, $\langle v_{\text{max}} \rangle$ (see details in Romanova et al. 2018). The bottom panel of Fig. 2 shows that the normalized time-averaged velocities, $\langle v_{\text{max}} \rangle / v_{\text{esc}}$, are approximately the same in the cases of smaller and larger boxes. We also calculated $v_{\text{max}} / v_{\text{esc}}$ and $\langle v_{\text{max}} \rangle / v_{\text{esc}}$ at different cylindrical boxes and observed that the ratio $\langle v_{\text{max}} \rangle / v_{\text{esc}}$ stays approximately constant (see middle panel of Fig. 3). The escape velocity decreases with distance, and therefore the poloidal velocity also decreases with distance. The right panel of Fig. 3 shows that the poloidal velocity decreases with distance approximately linearly. Approximating this dependence to larger distances from the star, we obtain $\langle v_{\text{max}} \rangle \approx 500$ km/s

⁷ We de-selected regions of very high velocity with low matter flux, by placing condition that the matter flux should be larger some small value, $\rho v_p = 0.001$ (in dimensionless units) (see details in Romanova et al. (2018) and Fig. 7 from this paper, which shows the position of the maximum poloidal velocity).

Model	$\langle \tilde{E}_f \rangle$	$\langle \tilde{E}_m \rangle$	$\langle \dot{E}_f \rangle$ (erg/s)
$\tilde{\mu}30$	0.59	0.07	$1.0\text{E}34 k_{0.2}$
$\tilde{\mu}60$	1.59	0.09	$9.1\text{E}33 k_{0.2}$

Table 4. Time-averaged energy fluxes to the wind carried from the surface of the star by the magnetic field and my matter. $\langle \tilde{E}_f \rangle$ and $\langle \tilde{E}_m \rangle$ are dimensionless and dimensional values, respectively.

at the distance of $r \approx 60R_s$. Overall, both the azimuthal and poloidal velocities decrease with distance and are expected to have lower values at larger distances from the star.

Propeller ejections are non-stationary and shock waves may form, where new ejecta interacts with a slower-moving matter of the earlier ejected matter. We suggest that the flares observed in optical, UV and X-ray spectral bands may be associated with radiation in these shocks and in the surrounding medium. To explain the relatively low velocities in radiating matter, one should consider distances that are two times (or more) greater than compared with our simulation region.

We should note that a small amount of matter is rapidly accelerated by the magnetic pressure force in regions, closer to the axis (see Fig. 4). These magnetic (Poynting flux) ejections do not correlate directly with the matter ejections. They occur during episodes of strong inflation of the magnetic loops. Ejections are non-stationary, and formation of shock waves is also expected. In shocks, the magnetic energy can be converted into the particle energy due to reconnection or other processes (e.g., Romanova & Lovelace 1992, Romanova & Lovelace 1997). These shocks may be responsible for radio flares and for the high-energy radiation. These magnetic outflows are magnetically-collimated and are expected to form the jet-like flow at larger distances from the star. They are similar to magnetic jets studied in compact stars and quasars (e.g., Ustyugova et al. 2000; Tchekhovskoy et al. 2012). We suggest that flaring radiation in radio band may originate in the shock waves of this jet. The similarity between the radio spectra of AE Aqr and that of microquasar Cyg X-3 is in favour of this hypothesis. Some part of the magnetic energy can be converted to the high-energy radiation. However, it can be a small, and therefore there is no contradiction with recent luck in finding TeV radiation from AE Aqr (e.g., Aleksić et al. 2004).

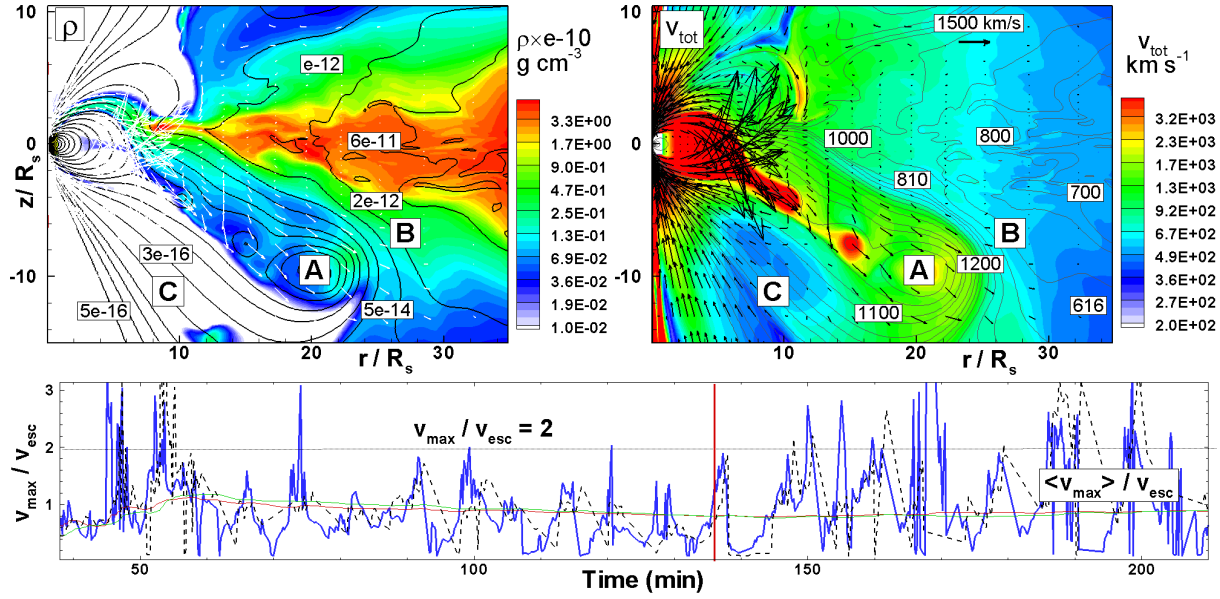


Figure 2. Top panels: Different characteristics of the flow during propeller ejection (at $t = 188$ min). Black lines are sample poloidal field lines, arrows are proportional to velocity vectors. The background in the left and right panels shows the density, ρ , and the absolute value of the total velocity, v_{tot} , respectively. Bottom panel: Temporal variation of the normalized maximum poloidal velocity, taken at cylinders with radii $r = 20R_s$ (blue line) and $r = 30R_s$ (dashed black line). Red and green lines show the time-averaged values, respectively. Vertical line shows the moment of time corresponding to top panels.

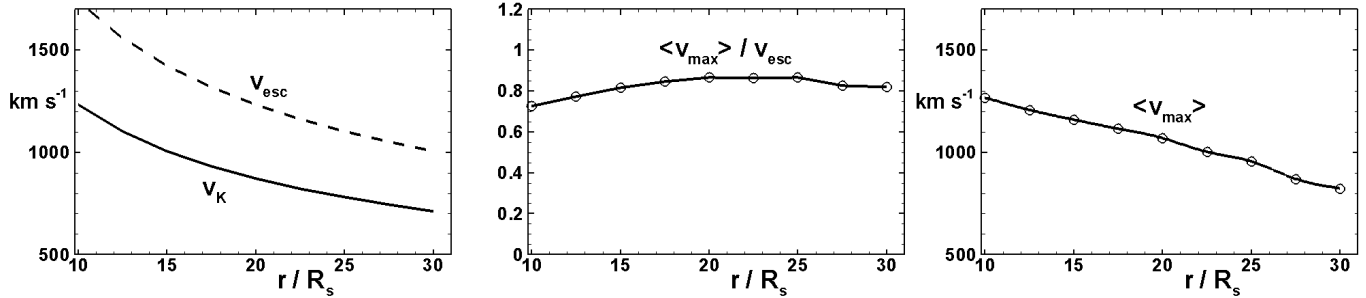


Figure 3. Left panel: Variation of Keplerian, v_K , and escape velocity, v_{esc} , with the distance from the star. Middle panel: Variation of the time-averaged maximum poloidal velocity normalized by the local escape velocity with the distance from the star. Right panel: Variation of the time-averaged maximum poloidal velocity with the distance from the star.

3.4 Time intervals between flares

Next, we compare the variability time scales obtained in our numerical models with the time scales observed in the light curves of AE Aqr. Fig. 3 from Mauche et al. (2012) shows that there are two types of flares: some flares occur rarely, with a time interval of a 1-3 hours between each flare (see individual large flares marked by vertical dashed lines); other flares occur more frequently, on time intervals of 10-30 minutes (see multiple flares on the left-hand side of Fig. 3 from Mauche et al. 2012, and also the sub-flares that occur on other time intervals). We can compare the observed time scales with the time scales obtained in our models.

Fig. 1 shows the variability obtained in model $\tilde{\mu}60$. The bottom panel shows the matter fluxes onto the star, \dot{M}_s , and into the wind, \dot{M}_w . The blue line in the top panel shows that the strongest ejections into the wind occur every 10-20 minutes. This time scale is similar to the time scales of the frequent flares in the observed light curve. Ejections into the

wind are slightly more frequent ($\sim 5 - 10$ min) in the model with the smaller magnetosphere, $\tilde{\mu}30$. Overall, the variability time scales match the short time scale oscillations in the observed light curve.

In our simulations, ejections into the wind occur in brief bursts, because outflows are only possible if the field lines connecting the star with the inner disc inflate and open. Inflation becomes possible when a sufficient amount of matter accumulates at the inner disc and diffuses through the field lines of the outer magnetosphere. Most of the time, matter is accumulated at the inner disc, while the outflow events are relatively brief. This is why the variability curve looks spiky (see bottom panel of Fig. 1). However, the small scale oscillations observed in AE Aqr are not spiky. We suggest that a proper inclusion of radiation in our model may change the shape of the variability curve, possibly making the oscillations less spiky.

On the other hand, the variability curve associated with the variation of the inner disc radius, r_m (see middle row of

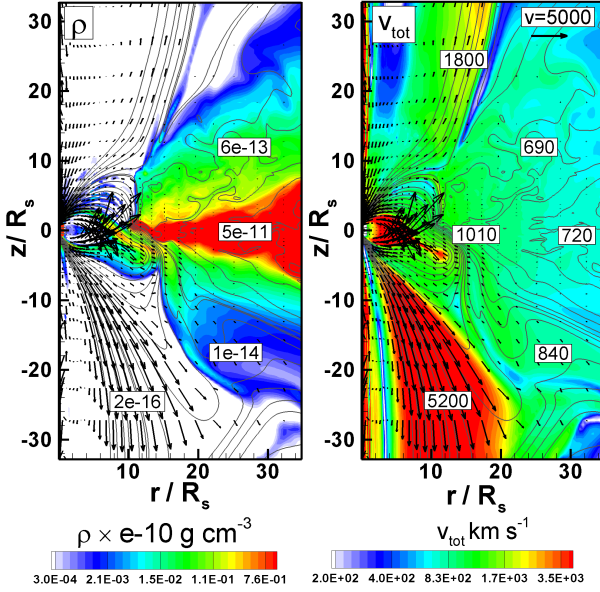


Figure 4. An example of outflows into the magnetic, Poynting flux jet. The meaning of the color background, vectors and lines is the same, as in top panels of Fig. 2.

Fig. 1), is not spiky. It strongly resembles the observed light curve for short time scale flares. In some theoretical models, it is suggested that the flaring radiation is connected with the processes at the disc-magnetosphere boundary and in the inner disc, such as the heating in the turbulent layer of the boundary (Papitto & Torres 2015), or the acceleration of particles in the magnetized plasma of the inner disc (Meintjes & de Jager 2000). If the radiation really does originate at the inner disc, then the oscillations of the inner disc (observed in our model) will lead to the variations in the observed light curves.

The origin of the less frequent flares in the light curves of AE Aqr may be connected with the non-stationary accretion expected in the propeller regime. On the other hand, non-stationary ejections can be due to the non-stationary accretion of matter from the secondary star, which may have the form of inhomogeneous streams, or blobs (e.g., Wynn & King 1995). More detailed analysis of these processes is beyond the scope of this paper.

3.5 Energy in Flares

A star loses its rotational energy. A part of this energy is transferred to the energy of the inner disc winds, while another part flows from polar regions of the star in the form of magnetic, Poynting flux jets. The time-averaged energy fluxes carried by matter (m) and by the magnetic field (f) through some surface $S(r, z)$ are:

$$\langle \dot{E}_{m,f} \rangle \approx 5.29 \times 10^{32} \tilde{\mu}_{60}^{-2} B_5^2 \langle \tilde{E}_{m,f} \rangle \text{ erg/s}, \quad (13)$$

where $\langle \tilde{E}_{m,f} \rangle$ are corresponding dimensionless values. Table 4 shows energy fluxes calculated at the stellar surface. One can see that almost all energy is carried by the magnetic field. A smaller amount of energy is carried by the matter, which accretes onto the star.

Observations of AE Aqr show aperiodic flares in optical, UV, X-ray and radio bands (e.g., Patterson 1979). Similar flares are observed in the UV spectrum (Eracleous & Horne 1996). The luminosity of flares in the high state in the Balmer continuum reaches the value of 8.4×10^{31} erg/s, and values a few times smaller in the low state in the Balmer continuum, and in the UV and Blamer spectral lines (see Tab. 3 from Eracleous & Horne 1996). The X-ray luminosity is lower, while the radio luminosity is much lower.⁸

In our model, matter is ejected from the inner disc into the wind in non-stationary bursts (see bottom panel of Fig. 1). The ejected matter is accelerated by the magnetic pressure force from zero velocity (near the disc) up to hundreds of km/s at larger distances (see Sec. 3.3). Accelerated chunks of matter, while interacting with earlier ejected matter, may form shock waves, and a significant part of the kinetic energy can be radiated in the shock waves and observed as flares⁹.

Matter is ejected from the inner disc in chunks of different mass. Using a plot in the bottom panel of Fig. 1, we can estimate the mass ejected in individual bursts. For example, at time $t = 123$ min, the large ejection lasted for $\Delta t \approx 120$ sec and the total integrated ejected mass is estimated as $\Delta M \approx 3 \times 10^{19}$ g. Smaller ejections have mass of $\Delta M \sim (0.3 - 1.0) \times 10^{19}$ g.

The kinetic energy, carried by individual chunks is

$$E_{\text{kin}} \approx \frac{1}{2} \Delta M v_p^2 \approx 3.7 \times 10^{34} \frac{\Delta M}{3 \times 10^{19} \text{ g}} \left(\frac{v_p}{500 \text{ km/s}} \right)^2 \text{ erg}$$

A typical duration of strong ejections is $\Delta t \approx 2$ min, and the rate of energy release during ejection is

$$\dot{E}_{\text{kin}} \approx \frac{E_{\text{kin}}}{\Delta t} \approx 3.1 \times 10^{32} \frac{\Delta M}{3 \times 10^{19} \text{ g}} \left(\frac{v_p}{500 \text{ km/s}} \right)^2 \frac{2 \text{ min}}{\Delta t} \frac{\text{erg}}{\text{s}}.$$

This rate of energy release is sufficient to explain the observed flares.

Our model can be compared with the model of colliding blobs (e.g., Wynn et al. 1997). In this model, it is suggested that matter accretes onto the magnetosphere in blobs, which are subsequently ejected by the propelling magnetosphere in clumps, which collide with each other and radiate (e.g., Pearson et al. 2003; Zamanov et al. 2012). To explain the observed flares, they estimate the mass involved in collisions as $\Delta M \approx 3 \times 10^{19}$ g and the total energy, released during collisions, as $E \approx 3 \times 10^{33}$ erg/s. It is interesting, that the mass of our largest ejections is similar to the mass in their model. However, they considered longer-lasting flares, while our flares are relatively brief.

In our model, energy also flows in the form of invisible magnetic energy. Some energy is associated with the magnetic field lines expanding together with matter into the inner disc wind. On the other hand, a significant amount of magnetic energy flows from the surface of the star along the inflated field lines in the form of a Poynting flux jet, where a small amount of matter is accelerated rapidly by the magnetic force. The Poynting flux outflows are non-stationary, and particles may be accelerated at the magnetic shocks (e.g., Romanova

⁸ Energetic flares in γ -rays were reported Meintjes et al. (1994), however were not confirmed by other groups.

⁹ In our code, the energy equation is written in the entropy form, and the shocks cannot be modelled.

& Lovelace 1997), possibly up to very high energies. However, it is not clear which part of the energy will propagate in the form of an invisible, magnetic jet and which part will be converted to accelerated particles and radiation¹⁰.

4 SUMMARY

In this work, we have developed a propeller model of AE Aqr using axisymmetric simulations. We suggested that some type of an accretion disc forms around the white dwarf and interacts with the magnetosphere of the star in the propeller regime. We compared the results of our models, $\tilde{\mu}30$ and $\tilde{\mu}60$, with the observations. In these models, the time-averaged magnetospheric radii are $\langle r_m \rangle \approx 5$ and 6, and the fastness parameter values are $\omega_s = 3.9$ and 5.1, respectively. Our conclusions are the following:

1. Both models can explain the rapid spin-down of AE Aqr, although at slightly-different values of the magnetic field of the white dwarf: $B_s \approx (2.9, 3.3) \times 10^5$ G for $\tilde{\mu} = 30$ and 60, respectively.

2. In both models, the disc-magnetosphere interaction is a strongly non-stationary process, where the inner disc oscillates. The total time-averaged accretion rate in the disc is $\dot{M}_d = (1.0, 0.55) \times 10^{17}$ g/s in the above two models, respectively.

3. Most of the inner disc matter is ejected into conically-shaped winds, and a much smaller part accretes onto the star. Our axisymmetric model is not precise in providing the accretion rate onto the star, due to unknown diffusivity rate.

4. The main flaring variability can be explained through the processes in the non-stationary outflows (possibly by the radiation in shocks). The time-averaged total energy budget in the outflows, 2×10^{33} erg/s, is sufficient for explaining the flares observed in different wavebands.

5. The predicted accretion rate onto a star is higher than that obtained from the observations of accretion luminosity of AE Aqr ($E_{\text{acc}} \lesssim 10^{32}$ erg/s). The relatively high accretion rate in our models can be explained by the high diffusivity at the disc-magnetosphere boundary, taken in our axisymmetric models.

6. Velocities of matter in the simulation region $v \sim 600 - 1,200$ km/s, are high and cannot explain the low velocity component of the flaring radiation observed in the H_α spectral line. Matter responsible for this flaring radiation should be located at least at twice as large distance from the star, compared with our simulation region.

7. Both accretion and ejections are non-stationary and occur in brief episodes. The ejections of matter into the outflows and the oscillations of the inner disc occur on a time

scale of $\Delta t \approx 10 - 20$ minutes. This variability matches the short time scale variability observed in the light curves of AE Aqr. The longer time scale variability may be connected with the non-stationary accretion from the disc.

Overall, the developed models of AE Aqr are in reasonable agreement with the observational data. One of the inconsistencies is the presence of an accretion disc in our model and no observational evidence of an accretion disc in the Doppler tomograms (e.g., Wynn et al. 1997). We should note that, in our models of the strong propeller regime, the inner disc strongly oscillates. This may lead to a variable, non-ordered disc, which can be difficult to detect using the Doppler tomography technique (which suggested a steady flow of matter in the equatorial plane of the binary, e.g., Echevarría 2012). Our propeller models work even in the cases where the disc is variable, relatively small, or when it forms as a temporary feature. Additionally, in our model, most of the disc matter is ejected into the outflows, which can distort information about the accretion disc in the Doppler tomograms.

Another important inconsistency of the model is the fact that the model provides a higher accretion rate onto the surface of a star compared with that derived from the observations. We should point out that our axisymmetric model we suggested a high diffusivity in the inner part of the simulation region (to mimic the 3D instabilities), which may lead to a higher accretion rate. On the other hand, in more realistic 3D simulations, the magnetic axis can be tilted about the rotational axis, which may lead to lower accretion rate onto the surface of the star in the propeller regime.

ACKNOWLEDGMENTS

The authors thank the anonymous referee for valuable comments and corrections, and Gagik Tovmassian for helpful discussion.

Resources supporting this work were provided by the NASA High-End Computing (HEC) Program through the NASA Advanced Supercomputing (NAS) Division at the NASA Ames Research Center and the NASA Center for Computational Sciences (NCCS) at Goddard Space Flight Center. The research was supported by NASA grant NNX14AP30G. AVK was supported by the RFBR grant 18-02-00907.

References

- Alexić, J., et al. 2014, A&A, 568, A109, pp. 1-8
- Armitage, P., 1998, ApJ, 501, L189
- Arons, J. & Lea, S.M. 1976, ApJ, 207, 914
- Balbus, S.A., & Hawley, J.F. 1991, ApJ, 376, 214
- Bastian, T. S., Dulk, G. A., & Chanmugam, G. 1988, ApJ, 324, 431
- Blinova, A. A., Romanova, M. M., Lovelace, R. V. E. 2016, MNRAS, 459, 2354
- Casares, J., Mouchet, M., Martínez-Pais, I.G., Harlaftis, E.T. 1996, MNRAS, 282, 182
- Choi, C.-S., Dotani, T., Agrawal, P. C. 1999, ApJ, 525, 399
- Choi, C.-S. and Yi, I. 2000, ApJ, 538, 862
- Cowling, T. G. 1934, MNRAS, 194, 39
- de Jager, H.I., de Jager, O. C., North, A. R., Raubenheimer,

¹⁰ Recent observations of the very high-energy radiation from AE Aqr, performed by *MAGIC* at the energies of > 100 GeV (Aleksić et al. 2004) and by *Fermi*-LAT in the 100 MeV-300 GeV energy range, have shown that this radiation, if present, should be weak, much weaker than that of $\sim 10^{34}$ erg/s reported in the earlier observations in the TeV band (e.g., De Jager et al. 1986). In our model, individual ejections into the Poynting flux jet may have the sufficiently high energy flux of $\sim 10^{34}$ erg/s. However, only a small part of this energy can be converted into the very high-energy radiation.

- B. C., van der Walt, D. J., van Urk, G., 1986, *South African Journal of Physics*, Vol. 9, No. 3, p. 107
- de Jager, O.C., 1994, *ApJS*, 90, 775
- de Jager, O.C., Meintjes, P.J., O'Donghue, D., Robinson, E.L., 1994, *MNRAS*, 267, 577
- de Martino, D., Belloni, T., Falanga, M., Papitto, A., Motta, S., Pellizzoni, A., Evangelista, Y., Piano, G., Masetti, N., Bonnet-Bidaud, J.-M., Mouchet, M., Mukai, K., Possenti, A. 2013, *A&A*, 550, A89, 16
- Dhillon V., 1996, in Evans A., Wood J. H., eds, *Cataclysmic variables and related objects*. Kluwer, Dordrecht, p. 3
- Echevarría, J., Smith, R. C. Costero, R., Zharikov, S. & Michel, R. 2008, *MNRAS*, 387, 1563
- Echevarría, J. 2012, *Mem. S.A.It.*, Vol. 83, 570
- 897
- Eracleous, M., Horne, K., Robinson, E. L., et al. 1994, *ApJ*, 433, 313
- Eracleous, M., & Horne, K. 1996, *ApJ*, 471, 427
- Gardiner, T. A., Stone, J. M. 2005, *Journal of Computational Physics*, 205, 509
- Ghosh, P. 2007, *Rotation and Accretion Powered Pulsars: World Scientific Series in Astronomy and Astrophysics – Vol. 10*. Edited by Pranab Ghosh. Published by World Scientific Publishing Co., Pte. Ltd., Singapore
- Ghosh, P., Lamb, F. K. 1978, *ApJ*, 223, L83
- Goodson, A. P., Winglee, R. M., & Böhm, K.-H. 1997, *ApJ*, 489, 1099
- Hawley, J. F. 2000, *ApJ*, 528, 462
- Hellier, C., 1996, *ApJ*, 471, 949
- Horne, K. 1999, *Annapolis Workshop on Magnetic Cataclysmic Variables*, ASP Conference Series, Volume 157, edited by Coel Hellier and Koji Mukai, 1999, p. 349
- Illarionov, A. F., & Sunyaev, R. A. 1975, *A&A*, 39, 185
- Ikhsanov, N.R. 1998, *A&A*, 338, 521
- Ikhsanov, N.R. 1999, *A&A*, 347, 915
- Ikhsanov, N.R., Neustroev, V. V., Beskrovnaya, N. G. 2004, *A&A*, 421, 1131
- Ikhsanov, N.R. 2006, 1975, *ApJ*, 640, L59
- Isakova, P. B., Ikhsanov, N. R., Zhilkin, A. G., Bisikalo, D. V., Beskrovnaya, N. G. 2016, *Astronomy Reports*, Volume 60, Issue 5, 498
- Itoh, K., Okada, S., Ishida, M., Kunieda, H. 2006, 2006, *ApJ*, 639, 397
- King, A. R. 1993, *MNRAS*, 261, 144
- Kitaguchi, T., et al. 2014, *ApJ*, 782:3 (7pp)
- Koldoba, A. V., Ustyugova, G. V., Lii, P. S., Comins, M. L., Dyda, S., Romanova, M. M., Lovelace, R. V. E. 2016, *New Astronomy*, 45, 60
- Kuijpers, J., Fletcher, L., Abada-Simon, M., Horne, K.D., Raadu, M.A., Ramsay, G., Steeghs, D. 1997, *A&A*, 322, 242
- Kulkarni, A., & Romanova, M.M. 2008, *MNRAS*, 386, 673
- Lii, P.S., Romanova, M.M., Ustyugova, G.V., Koldoba, A.V., Lovelace, R.V.E. 2014, *MNRAS*, 441, 86
- Lovelace, R.V.E., Romanova, M.M., & Bisnovatyi-Kogan, G.S. 1999, *ApJ*, 514, 368
- Mauche, C.W. 2006, *MNRAS*, 369, 1983
- Mauche, C.W. 2009, *ApJ*, 706, 130
- Mauche, C. W., Abada-Simon, M., Desmurs, J.-F., Dulude, M. J., Ioannou, Z., Neill, J. D., Price, A., Sidro, N., Welsh, W. F., AAVSO CBA, 2012, *Memorie della Societa Astronomica Italiana*, v.83, p.651
- Marsh T. R., Home K, Schlegel E. M., Honeycutt R. K, Kaitchuk R. H., 1990, *ApJ*, 364, 637
- Meintjes, P.J., de Jager, O. C., Raubenheimer, B. C., Nel, H. I., North, A. R., Buckley, D. A. H., Koen, C. 1994, *ApJ*, 434, 292
- Meintjes, P.J., & de Jager, O.C. 2000, *MNRAS*, 311, 611
- Papitto, A., & Torres, D.E. 2015, *ApJ*, 807, article id. 33, 10 pp.
- Patterson, J. 1979, *ApJ*, 234, 978
- Patterson, J., Branch, D., Chingaringi, G., & Robinson, E. L. 1980, *ApJ*, 240, L133
- Pearson, K.J., Horne, K., Skidmore, W. 2003, *MNRAS*, 338, 1067
- Pringle, J.E., & Rees, M.J. 1972, *A&A*, 21, 1
- Rodrigues, C., da Silva, K., Luna, G., Coelho, J., Lima, I., Costa, J., de Araujo, J. 2017, “The X-ray Universe 2017”, *Proceedings of the conference held 6-9 June, 2017 in Rome, Italy*. Edited by J.-U. Ness and S. Migliari.
- Romanova, M.M. & Lovelace, R.V.E. 1997, *A&A*, 262, 26
- Romanova, M.M. & Lovelace, R.V.E. 1997, *ApJ*, 475, 97
- Romanova, M.M., Kulkarni, A.K., Lovelace, R.V.E. 2008, *ApJ*, 673, L171
- Romanova, M.M. & Kulkarni, A.K. 2009, *MNRAS*, 398, 701
- Romanova, M.M. & Lovelace, R.V.E. 1997, *ApJ*, 475, 97
- Romanova, M.M. & Owocki, S.P. 2015, *Space Sciences Reviews*, Vol. 191, Issue 1-4, 339
- Romanova, M. M., Ustyugova, G. V., Koldoba, A. V., Lovelace, R. V. E., 2002, *ApJ*, 578, 420
- Romanova, M. M., Ustyugova, G. V., Koldoba, A. V., Lovelace, R. V. E., 2004, *ApJ*, 616, L151
- Romanova, M. M., Ustyugova, G. V., Koldoba, A. V., Lovelace, R. V. E., 2005, *ApJ*, 635, 165L
- Romanova, M. M., Ustyugova, G. V., Koldoba, A. V., Lovelace, R. V. E., 2009, *MNRAS*, 399, 1802
- 2011, *MNRAS*, 416, 416
- 2012, *MNRAS*, 421, 63
- Romanova, M. M., Blinova, A.A., Ustyugova, G. V., Koldoba, A. V., Lovelace, R. V. E., 2018, *New Astronomy*, 62, 94
- Schmidtobreick, L. 2015, *Proceedings of The Golden Age of Cataclysmic Variables and Related Objects - III (Golden2015)*, e-print: arXiv:1705.09332
- Schwöpe, A. D., Schwarz, R., Staude, A., Heerlein, C., Horne, K., Steeghs, D. 1999, *ASP Conference Series*, Volume 157, edited by Coel Hellier and Koji Mukai, p. 71
- Seaquist, E.R. 1993, *Rep. Prog. Phys.*, 56, 1145
- Schwöpe, A. D., Schwarz, R., Staude, A., Heerlein, C., Horne, K., Steeghs, D. 1999, *Annapolis Workshop on Magnetic Cataclysmic Variables*, ASP Conference Series, Volume 157, edited by Coel Hellier and Koji Mukai, 1999, p. 71
- Shakura, N.I., & Sunyaev, R.A. 1973, *A&A*, 24, 337
- Stone, J. M., Hawley, J. F., Gammie, C. F., Balbus, S. A. 1996, *ApJ*, 463, 656
- Sunyaev, R.A., & Shakura, N.I. 1977, *Pisma Astron. Zh.*, 3, 262
- Tchekhovskoy, A., McKinney, J. C., Narayan, R. 2012, *Journal of Physics: Conference Series*, Volume 372, Issue 1, id. 012040
- Thorstensen, J. R., Ringwald, F. A., Wade, R. A., Schmidt, G. D., Norsworthy, J. E. 1991, *AJ*, 102, 272 381
- Ustyugova, G.V., Koldoba, A.V., Romanova, M.M., Lovelace, R.V.E. 2006, *ApJ*, 646, 304
- Ustyugova, G.V., Lovelace, R.V.E., Romanova, M.M., Li, H., S.A. Colgate 2000, *ApJ*, 541, L21

- Wang, Y.-M.; Robertson, J. A. 1985, A&A, 151, 361
- Warner, B. 1995, “Cataclysmic Variable Stars”. Cambridge Astrophysics Series, Cambridge, New York: Cambridge University Press
- Welsh, W.F., Horne, K., and Gomer, R. 1993, ApJ, 410, L39
- Welsh, W.F., Horne, K., and Gomer, R. 1998, MNRAS, 298, 285
- Wynn, G. A., & King, A. R., 1995, MNRAS, 275, 9
- Wynn, G. A., King, A. R., & Horne, K. 1997, MNRAS, 286, 436
- Zamanov, R. K., Latev, G. Y., Stoyanov, K. A., Boeva, S., Spassov, B., Tsvetkova, S. V. 2012, Astronomische Nachrichten, Vol.333, Issue 8, p.736

APPENDIX A: DESCRIPTION OF NUMERICAL MODEL

A1 Initial and boundary conditions

The initial conditions are similar to those used in our previous work (Romanova et al. 2018), where the initial density and entropy distributions were calculated by balancing the gravitational, centrifugal and pressure forces. The disc is initially cold and dense, with temperature T_d and density ρ_d . The corona is hot and rarified, with temperature $T_c = 3 \times 10^3 T_d$ and density $\rho_c = 3.3 \times 10^{-4} \rho_d$. In the beginning of the simulations, the inner edge of the disc is placed at $r_d = 10$, and the star rotates with $\Omega_i = 0.032$ (corresponding to $r_{\text{cor}} = 10$), so that the magnetosphere and the inner disc initially corotate. This condition helps to ensure that the magnetosphere and the disc are initially in near-equilibrium at the disc-magnetosphere boundary. The star is gradually spun up from Ω_i to the final state with angular velocity $\Omega_s \approx 0.35$, which corresponds to $r_{\text{cor}} = 2$.

Initially, the disc is threaded by the dipole magnetic field of the star. We also add a small “tapered” poloidal field inside the disc. This tapered field helps initialize the MRI in the disc and has the same polarity as the stellar field at the disc-magnetosphere boundary. To initialize the MRI, 5% velocity perturbations are added to v_ϕ inside the disc.

the boundary conditions are identical to those described by Lii et al. (2014).

A2 Grid and code description

We use a Godunov-type code to solve the MHD equations in cylindrical coordinates (Koldoba et al. 2016). The axisymmetric grid is in cylindrical (r, z) coordinates with mesh compression towards the equatorial plane and the z -axis, so that there is a larger number of cells in the disc plane and near the star. In the models presented here, we use a non-uniform grid with 190×306 grid cells, corresponding to a grid that is 36 by 66 stellar radii in size.

A3 Reference values

We find the reference pressure from the relationship $p_0 = B_0^2$, where $B_0 = B_s/\tilde{\mu}$ is the reference magnetic field (B_s is the magnetic field of the star and $\tilde{\mu}$ is the dimensionless magnetic moment of the star). The reference density is $\rho_0 = p_0/v_0^2$, and the reference temperature is $T_0 = \mathcal{R}p_0/\rho_0$, where \mathcal{R} is the

Parameters	Reference Values
$M_0 [M_\odot]$	0.8
$R_0 [\text{cm}]$	7×10^8
$v_0 [\text{km s}^{-1}]$	3.90×10^3
$P_0 [\text{s}]$	11.26
$B_0 [\text{G}]$	$1.67 \times 10^3 \tilde{\mu}_{60}^{-1} B_5$
$\rho_0 [\text{g cm}^{-3}]$	$1.82 \times 10^{-11} \tilde{\mu}_{60}^{-2} B_5^2$
$n_0 [1 \text{ cm}^{-3}]$	$1.09 \times 10^{13} \tilde{\mu}_{60}^{-2} B_5^2$
$T_0 [\text{K}]$	1.83×10^9
$T_{\text{disc},0} [\text{K}]$	6.11×10^5

Table A1. Reference values for CV AE Aqr. Many of the reference values depend on the (unknown) value of the magnetic field of the star, B_s , and the dimensionless magnetic moment $\tilde{\mu} = 60$.

Rydberg constant. Table A1 shows different reference values and their dependencies on B_s and $\tilde{\mu}$.

Using the main reference values, we can calculate the reference values for the fluxes: matter flux, $\dot{M}_0 = \rho_0 v_0 R_0^2$, angular momentum flux, $\dot{L}_0 = \dot{M}_0 v_0 R_0$, and energy flux, $\dot{E}_0 = \dot{M}_0 v_0^2$. Taking into account the fact that $\rho_0 v_0 R_0^2 = B_0^2/v_0^2 = (B_s/\tilde{\mu})^2 (R_0^2/v_0)$, we obtain the reference fluxes in the following form:

$$\dot{M}_0 \approx 3.47 \times 10^{15} \tilde{\mu}_{60}^{-2} B_5^2 \text{ g/s}, \quad (\text{A1})$$

$$\dot{L}_0 \approx 9.53 \times 10^{32} \tilde{\mu}_{60}^{-2} B_5^2 \text{ erg}, \quad (\text{A2})$$

$$\dot{E}_0 \approx 5.29 \times 10^{32} \tilde{\mu}_{60}^{-2} B_5^2 \text{ erg/s}. \quad (\text{A3})$$